Chemical Science

ROYAL SOCIETY OF CHEMISTRY

EDGE ARTICLE

View Article Online
View Journal

Cite this: DOI: 10.1039/d5sc07619f

All publication charges for this article have been paid for by the Royal Society of Chemistry

Accelerated confined mass transfer in piezoelectric semiconducting metal–organic frameworks for H_2O_2 piezo-photosynthesis

Yuchen Lan,[a] Ling Gao,[b] Jin Qian,[a] Jinzhou Liu,[a] Bo Shen,[a] Menghao Yang,[b] Wenguang Tu,[c] Jiwei Zhai *[a] and Guanyu Liu*[a]

The piezo-photocatalytic O_2 reduction reaction offers a promising pathway towards H_2O_2 synthesis. However, in addition to rapid recombination of photogenerated electrons and holes, this gas-consuming reaction is inherently limited by O_2 dissolution and mass transfer dynamics. Here, energy band structures and dipole moments of piezoelectric semiconducting UiO-66 metal–organic frameworks (MOFs) are engineered by modulating functional groups ($-NH_2$, $-CH_3$, $-OH$, $-NO_2$ and $-F_4$) and metal nodes (Hf and Zr). This fine-tuning of MOF building blocks leads to an enhanced piezoelectric coefficient, gas capacity and light absorption to facilitate subsequent piezo-photocatalysis. Furthermore, the tunable band structure enables the construction of a Z-scheme heterojunction with another piezoelectric semiconductor. The resulting heterostructure CdS/NH_2-UiO-66(Hf) with increased structural asymmetry exhibits further boosted piezoelectricity, leading to rapid charge separation and transfer due to the enhanced piezoelectric-induced built-in electric field. In addition, the piezoelectric semiconducting MOF serves as a tri-functional nanoreactor synergistically improving gas solubility, confined mass transfer, and O_2 molecule activation under periodic piezoelectric deformation. Consequently, a H_2O_2 yield rate of 2079.1 μmol g^{-1} h^{-1} is achieved without sacrificial agents or O_2 bubbling *via* coupling of piezocatalytic and photocatalytic effects. This study opens a new avenue for tailoring microenvironments to design highly efficient piezo-photocatalytic systems.

Received 1st October 2025
Accepted 5th November 2025

DOI: 10.1039/d5sc07619f

rsc.li/chemical-science

1. Introduction

Photocatalytic hydrogen peroxide (H_2O_2) production through the two-electron oxygen reduction reaction (ORR) is a sustainable alternative to the energy-intensive anthraquinone process without hazardous by-products.[1–4] Typically, this photocatalytic process is driven using traditional semiconductors by absorbing photons with energy exceeding their bandgap to generate electron–hole pairs, which subsequently migrate to the surface to catalyze redox reactions. Recently, piezoelectric semiconductors have emerged as building blocks to construct piezoelectric-assisted photocatalytic systems taking advantage of both piezoelectric and photocatalytic effects. Specifically, under mechanical stress, piezoelectric photocatalysts with polarity develop a built-in electric field through spatially separated positive and negative charges, which facilitates the separation of photo-generated electron–hole pairs.[5–7] Consequently, piezoelectric semiconducting materials, such as ZnO,[5,8] $BaTiO_3$,[9,10] C_xN_y,[11,12] and covalent organic frameworks[13] have been investigated for H_2O_2 synthesis through optimization strategies including doping,[14] metal nanoparticle/single-atom decoration,[15] construction of heterojunctions,[16] crystal facet engineering,[17] *etc.*

Recently, cadmium sulphide (CdS), as a typical piezoelectric semiconductor with excellent visible-light absorption, suitable energy band levels, structural versatility, and good piezoelectric response, has also been reported to catalyze the ORR to form H_2O_2.[18–22] However, the aqueous-phase ORR as a gas-consuming reaction is fundamentally constrained by O_2 dissolution dynamics, where inadequate reactant delivery to catalytically active sites leads to mass-transport bottlenecks.[23,24] Accordingly, porous architectures, such as hollow carbon spheres and zeolite, have been engineered to construct macroporous/microporous water to enhance gas solubilities.[24–27] This strategy thereby establishes gas-enriched microenvironments at the catalyst–water interfaces, which is favorable for the gas-consuming reaction.[25–28]

Therefore, piezoelectric semiconducting metal organic frameworks (MOFs) with tailored micropores may enable

[a]Key Laboratory of Advanced Civil Engineering Materials of Ministry of Education, Functional Materials Research Laboratory, School of Materials Science and Engineering, Tongji University, Shanghai 201804, China. E-mail: apzhai@tongji.edu.cn; gyliu@tongji.edu.cn

[b]Shanghai Key Laboratory for R&D and Application of Metallic Functional Materials, Institute of New Energy for Vehicles, School of Materials Science and Engineering, Tongji University, Shanghai 201804, China

[c]School of Science and Engineering, The Chinese University of Hong Kong (Shenzhen), Shenzhen 518172, China

improved piezo-photocatalytic ORR to generate H_2O_2.[6,29,30] Furthermore, as piezoelectric pumps have been used in microfluidics, piezoelectric MOFs can potentially act as peristaltic nano-pumps to expedite the gas diffusion process within the confined microporous water upon external force-induced deformation. Hence piezoelectric semiconducting MOFs could serve as multifunctional nanoreactors synergistically integrating gas confinement, directional mass transport, and catalytic activation within their well-defined and tailorable structures. Notwithstanding this, the application of MOFs in piezo-photocatalytic gas-consuming reactions is scarcely reported.[31] UiO-66 is a prototypical zirconium-based MOF, characterized by its high stability, large surface area and tunable pore size. These properties make it highly promising for applications in gas storage/separation, catalysis, sensing, drug delivery, and photochemistry.[32–34] Notably, Zeng and co-workers demonstrated that UiO-66 nanocrystals often adopt a low-symmetry, non-centrosymmetric structure, which endows them with piezoelectric properties.[35] Given that the piezoelectricity of MOFs is governed by their polarity, density functional theory (DFT) calculations, well-suited for quantifying the changes in dipole moment induced by varying metal nodes and linker substituents, have been reported to reveal the underlying polarity and piezoelectricity differences.[6,30] Therefore, systematic investigation on piezoelectric semiconducting UiO-66 MOFs with tunable piezoelectricity, optical properties and porosity plays a pivotal role in elucidating structure–property relationships in piezo-photocatalytic systems.

Herein, a range of UiO-66 MOFs with different functional groups and metal nodes, with dipole moment determined by DFT calculations, were comprehensively examined. The synergistic variations in piezoelectricity, bandgap and specific surface area (SSA) emerge as the critical determinant governing their piezo-photocatalytic ORR performance. Upon integration with another piezoelectric semiconductor cadmium sulfide (CdS), the resulting structural asymmetric heterostructure demonstrated further increased piezoelectricity, resulting in enhanced separation and transport of photogenerated charge carriers owing to the piezoelectric-induced built-in electric field. The piezoelectric semiconducting MOF not only improved gas capacities and diffusion kinetics upon periodic deformation, but also activated the confined O_2 molecules towards O_2^- formation. As a result, the CdS/MOF heterostructure achieved a H_2O_2 yield rate of 2079.1 μmol g^{-1} h^{-1} from air and water under concurrent excitation of light and ultrasonication. This work sheds light on the potential of piezoelectric semiconducting porous materials to break the bottleneck of photocatalytic gas-consuming reactions by improving gas solubility and mass transfer.

2. Results and discussion

2.1. Effects of functional groups and metal nodes on UiO-66 piezo-MOFs

First, a series of M-UiO-66(Zr)/(Hf) (M = blank, NH_2, CH_3, OH, NO_2 and F_4) MOFs with different functional groups and metal nodes were synthesized. To further establish heterostructures, they undergo heat treatment with CdS in the subsequent synthesis process (*vide infra*). Therefore, the MOFs upon calcination at the temperature for heterostructure construction were denoted as NH_2-UiO-Hf, UiO-Hf, NH_2-UiO-Zr, F_4-UiO-Hf, CH_3-UiO-Zr, OH-UiO-Zr, NO_2-UiO-Zr, UiO-Zr and F_4-UiO-Zr, respectively. Powder X-ray diffraction (XRD) analysis confirmed the similar crystalline structures of the nine UiO-66-based MOFs (Fig. S1 and 1a). By comparing the XRD patterns and Fourier transform infrared (FTIR) spectra of the nine MOFs before and after calcination, UiO-Hf, CH_3-UiO-Zr, OH-UiO-Zr, NO_2-UiO-Zr, UiO-Zr and F_4-UiO-Zr reveal no obvious change before and after calcination with good thermal stability (Fig. S1 and S2). Nevertheless, NH_2-UiO-Hf, NH_2-UiO-Zr and F_4-UiO-Hf show broadening of the crystalline peaks after calcination, indicating disruptive effects on their crystalline structures. Fig. S3 shows their morphologies including the nanoparticulate structure for NH_2-UiO-Hf, UiO-Hf, NH_2-UiO-Zr, CH_3-UiO-Zr, OH-UiO-Zr, NO_2-UiO-Zr, and UiO-Zr and nanoflakes for F_4-UiO-Hf and F_4-UiO-Zr. Nitrogen adsorption–desorption measurements show that NH_2-UiO-Hf, NH_2-UiO-Zr and OH-UiO-Zr have similar Brunauer–Emmett–Teller (BET) surface areas of 397.6 m^2 g^{-1}, 322.9 m^2 g^{-1} and 315.2 m^2 g^{-1}, respectively. UiO-Zr and UiO-Hf show the largest BET surface area of 949.2 m^2 g^{-1} and 836.7 m^2 g^{-1}, respectively, whereas F_4-UiO-Hf and F_4-UiO-Zr show the smallest SSA of 261.6 m^2 g^{-1} and 262.4 m^2 g^{-1}, respectively (Fig. 1b and S4a). Despite the variation of SSA amongst the nine piezoelectric MOFs, their pore size distributions are similar, with an average pore size of 1.6 nm for NH_2-UiO-Hf, NH_2-UiO-Zr, F_4-UiO-Hf, CH_3-UiO-Zr, OH-UiO-Zr, NO_2-UiO-Zr, UiO-Zr, and F_4-UiO-Zr, and 1.8 nm for UiO-Hf (Fig. S5a and b). The light absorption was measured using UV-vis diffuse reflectance spectroscopy (UV-vis DRS), as shown in Fig. 1c and S4b. It can be deduced that their absorption edges are at 466.2 nm, 311.6 nm, 455.9 nm, 339.7 nm, 335.1 nm, 378.0 nm, 392.4 nm, 318.7 nm and 369.0 nm, with the corresponding bandgaps of 2.66 eV, 3.98 eV, 2.72 eV, 3.65 eV, 3.70 eV, 3.28 eV, 3.16 eV, 3.89 eV and 3.36 eV based on the Tauc plots (Fig. S5c and d). Subsequently, their piezoelectric properties were investigated using piezo-response force microscopy (PFM) as shown in Fig. 1d and S6. The piezoelectric hysteresis curves exhibit a typical butterfly shape under a ±10 V DC bias electric field with phase changes of 180° in all samples. The effective piezoelectric coefficients d_{33} of NH_2-UiO-Hf, UiO-Hf, NH_2-UiO-Zr, F_4-UiO-Hf, CH_3-UiO-Zr, OH-UiO-Zr, NO_2-UiO-Zr, UiO-Zr and F_4-UiO-Zr are determined to be 78.31, 50.31, 39.15, 36.55, 33.46, 34.03, 47.51, 49.45 and 27.64 pm V^{-1}. To further unravel the effect of different functional groups and metal nodes on the piezoelectricity of the UiO-66 MOFs (Fig. S7), the dipole moments of four model MOFs were calculated using DFT. The 2D ELF basin analyses of NH_2-UiO-66(Hf), UiO-66(Hf), NH_2-UiO-66(Zr) and F_4-UiO-66(Hf) are shown in Fig. 1e. The dipole moments of NH_2-UiO-66(Hf), UiO-66(Hf), NH_2-UiO-66(Zr) and F_4-UiO-66(Hf) were calculated to be −0.012, −0.006, −0.010 and −0.005 eÅ, respectively (Fig. 1f). The dipole moment of NH_2-UiO-66(Hf) is larger than that of UiO-66(Hf), suggesting that the introduction of the –NH_2 functional group enhances the polarity. The –F_4 group, in contrast, weakened the polarity of the MOF. Meanwhile,

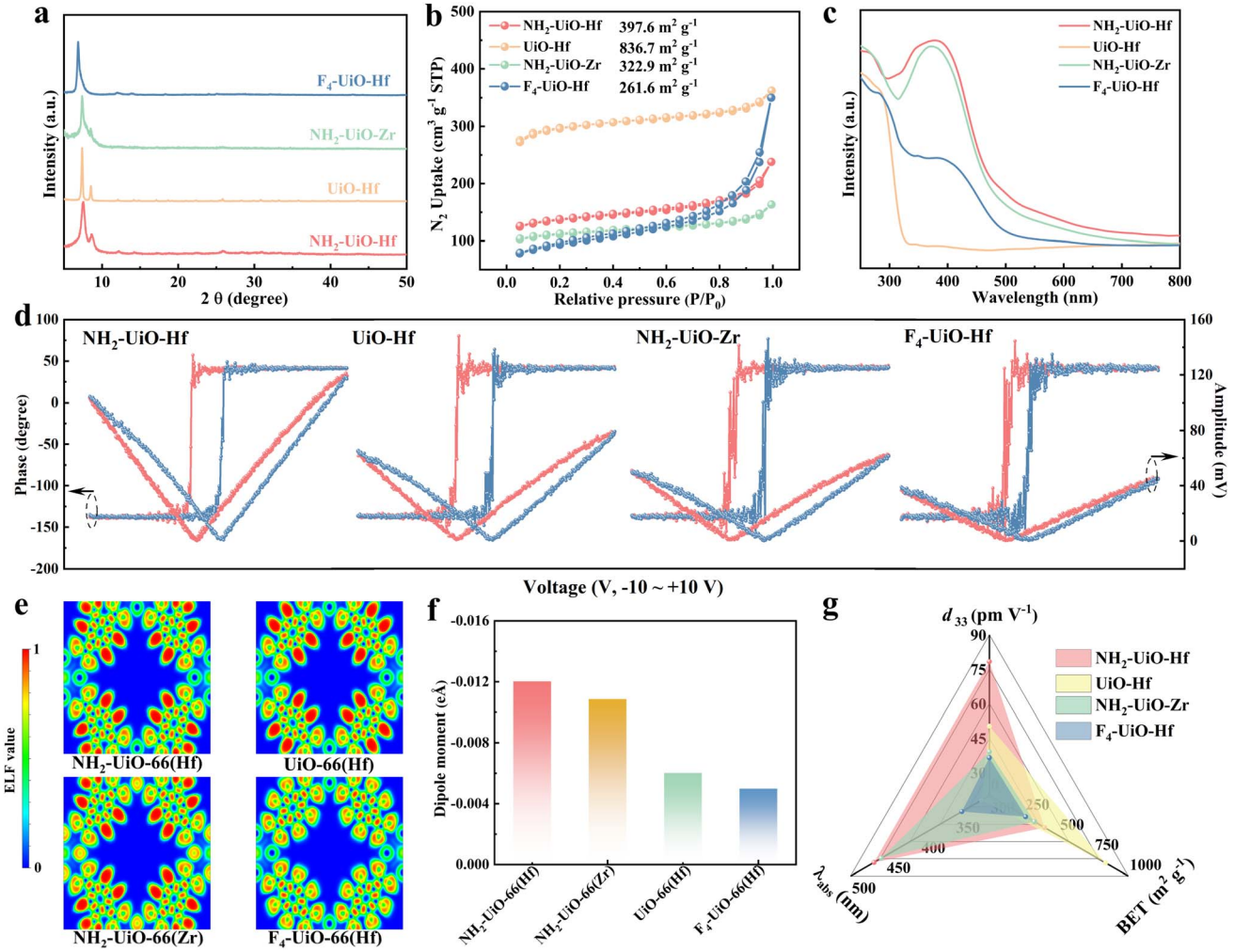

Fig. 1 (a) XRD patterns of NH_2-UiO-Hf, UiO-Hf, NH_2-UiO-Zr and F_4-UiO-Hf upon calcination. (b) Nitrogen adsorption–desorption isotherms of NH_2-UiO-Hf, UiO-Hf, NH_2-UiO-Zr and F_4-UiO-Hf. (c) UV-vis DRS of NH_2-UiO-Hf, UiO-Hf, NH_2-UiO-Zr and F_4-UiO-Hf. (d) Piezoresponse amplitude–voltage and phase hysteresis loops of NH_2-UiO-Hf, UiO-Hf, NH_2-UiO-Zr and F_4-UiO-Hf. (e) 2D ELF basin analyses of NH_2-UiO-66(Hf), UiO-66(Hf), NH_2-UiO-66(Zr) and F_4-UiO-66(Hf). (ELF value: 0 = fully delocalized, 1 = fully localized). (f) The corresponding calculated dipole moments. (g) Comparisons of the key parameters amongst NH_2-UiO-Hf, UiO-Hf, NH_2-UiO-Zr and F_4-UiO-Hf.

NH_2-UiO-66(Hf) has a larger dipole moment than NH_2-UiO-66(Zr), which could be ascribed to the larger polarity of the Hf–O bond than that of the Zr–O bond.[36–38] It is noteworthy that the minor inconsistency of the trend between the calculated dipole moments and measured d_{33} could be due to the aforementioned disruptive effects upon calcination on their original structures. To conduct a comprehensive comparison, the key parameters of these MOFs with different functional groups and metal nodes are summarised in Fig. 1g, including SSA, d_{33} and light absorption edges. Notably, NH_2-UiO-Hf demonstrates well-balanced properties in all three metrics, which could be promising for piezo-photocatalysis as a microporous piezoelectric semiconductor.

2.2. Structural characterization of the CdS/NH_2-UiO-Hf heterostructure

A CdS/NH_2-UiO-Hf heterostructure was synthesized *via* a hydrothermal and post-assembly method (Fig. S8) and subsequently characterized by XRD (Fig. 2a). The XRD pattern of CdS/NH_2-UiO-Hf contains diffraction peaks of both CdS and NH_2-UiO-Hf, which confirms the successful synthesis of heterostructures. This result is also observed in the XRD patterns of the heterostructure with various MOF contents, as the intensity of the two low-angle diffraction peaks of NH_2-UiO-Hf gradually increases with the increasing MOF weight percentage (Fig. S9). Moreover, Raman and FTIR spectra of CdS/NH_2-UiO-Hf also manifest that the individual CdS and MOF structure was maintained in the heterostructure (Fig. S10). In this designed heterostructure, piezo-MOF can serve as a gas reservoir by creating microporous water with high gas solubilities,[26] with its piezoelectricity accelerating the gas diffusion process under mechanical vibration. Moreover, the CdS/NH_2-UiO-Hf piezoelectric semiconductor heterojunction will facilitate the separation and transport of photogenerated electrons/holes especially under the piezoelectric-induced built-in electric field, to participate in the subsequent redox reactions.

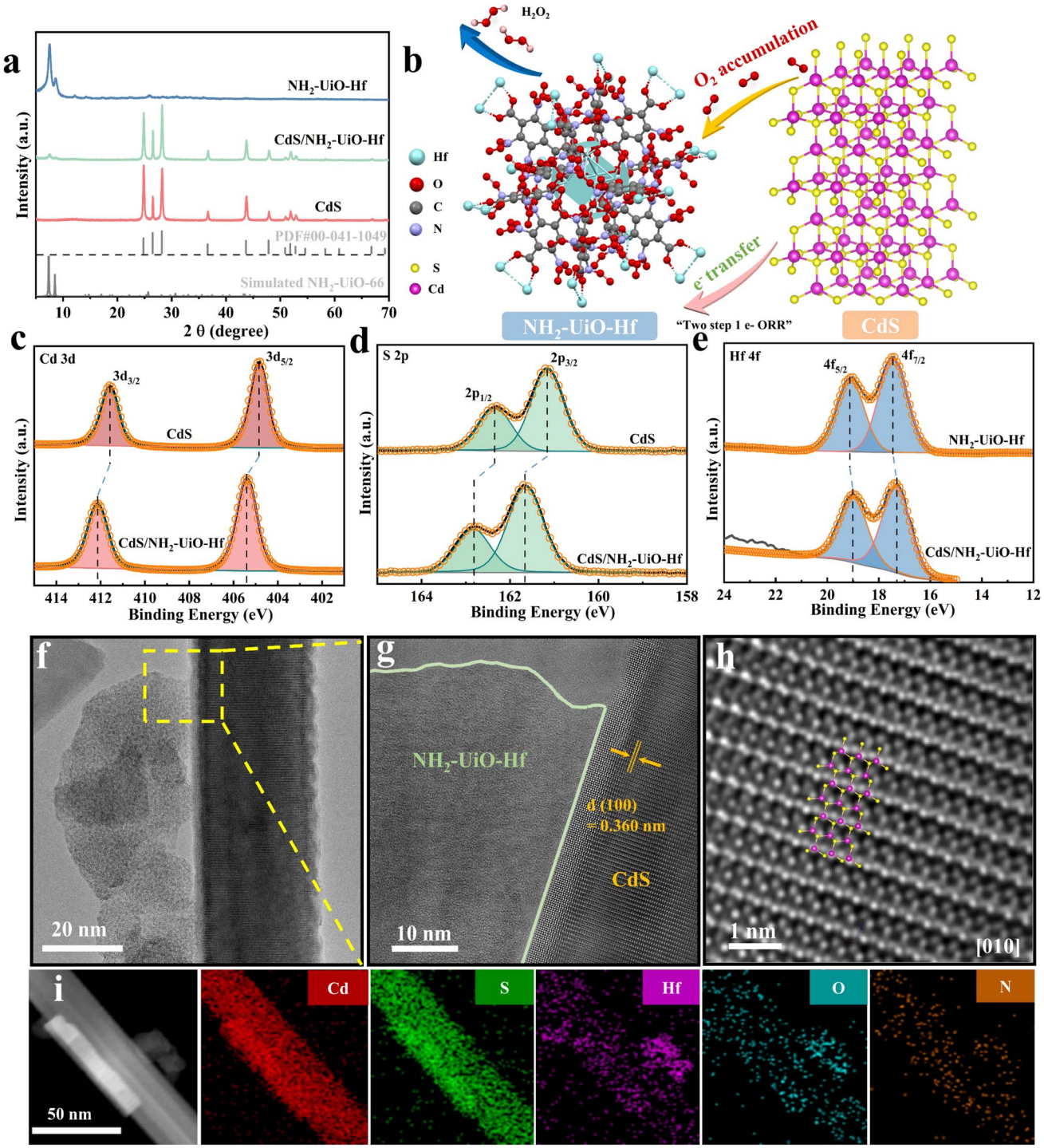

Fig. 2 (a) XRD patterns of NH_2-UiO-Hf, CdS and CdS/NH_2-UiO-Hf. (b) Proposed piezo-photocatalytic reaction mechanism for the CdS/NH_2-UiO-Hf heterostructure. High-resolution XPS spectra of (c) Cd 3d, (d) S 2p, and (e) Hf 4f in CdS, NH_2-UiO-Hf and CdS/NH_2-UiO-Hf. (f) HRTEM image of CdS/NH_2-UiO-Hf. (g) Enlarged HRTEM image of the yellow square. (h) HRTEM image of CdS in the heterostructure. (i) Corresponding elemental mapping of CdS/NH_2-UiO-Hf.

Fig. 2b illustrates the possible catalytic reaction pathways and mechanisms involved in the CdS/NH_2-UiO-Hf heterostructure.

As shown in X-ray photoelectron spectroscopy (XPS) results (Fig. 2c–e), the characteristic peaks of Cd 3d and S 2p in CdS/NH_2-UiO-Hf were shifted to high binding energies in comparison with CdS, whereas the binding energy of Hf 4f in the heterostructure, as compared to NH_2-UiO-Hf, exhibits a negative shift of 0.2 eV. The shifting in their XPS spectra suggests electron transfer from CdS to NH_2-UiO-Hf.[22,39] The morphological features obtained by scanning electron

microscopy (SEM) show that nanorod-like CdS displays an average length of 200–1000 nm (Fig. S11a), whereas NH_2-UiO-Hf consisted of octahedral-like particles with a feature size of around 40 nm (Fig. S11b). In CdS/NH_2-UiO-Hf, the octahedral-like NH_2-UiO-Hf particles are uniformly decorated on the CdS nanorods upon post-assembly (Fig. S11c). The heterostructure and elemental distributions were further analysed using high-resolution transmission electron microscopy (HRTEM). NH_2-UiO-Hf, as shown in the dashed yellow square, is tightly attached to the smooth surface of CdS nanorods with intimate interface contact marked as a green line (Fig. 2f and g). In addition, CdS shows distinct lattice fringes with an interplanar spacing of 0.36 nm, corresponding to the (100) crystal plane of hexagonal wurtzite CdS (Fig. 2h).[40] Energy-dispersive X-ray spectroscopy (EDS) elemental mapping confirms the coexistence of Cd, Hf, S, N and O, revealing distinct spatial segregation that aligns with the designed heterostructure (Fig. 2i). Specifically, Cd and S are mainly distributed in the nanorod-like region, while Hf, N and O elements are predominantly localized within the rectangle-shaped particle region on the right side.

2.3. Piezo-photocatalytic performance evaluation

The performance of all catalysts was assessed for H_2O_2 production under light radiation and/or ultrasonic vibration in deionized water without O_2 bubbling and sacrificial agents (Fig. S12). First, the H_2O_2 production under catalyst-free conditions was negligible (Fig. S13). The piezo-, photo-, and piezo-photocatalytic performance of CdS/NH_2-UiO-Hf with various weight percentages of NH_2-UiO-Hf was examined, with the 15 wt% as the best-performing sample (Fig. S14). The H_2O_2 concentration using CdS, NH_2-UiO-Hf and CdS/NH_2-UiO-Hf catalysts exhibited quasi-linear accumulation over time, with good stability throughout the measurement period (Fig. 3a–c). As shown in Fig. 3d, the H_2O_2 yield rates of CdS/NH_2-UiO-Hf

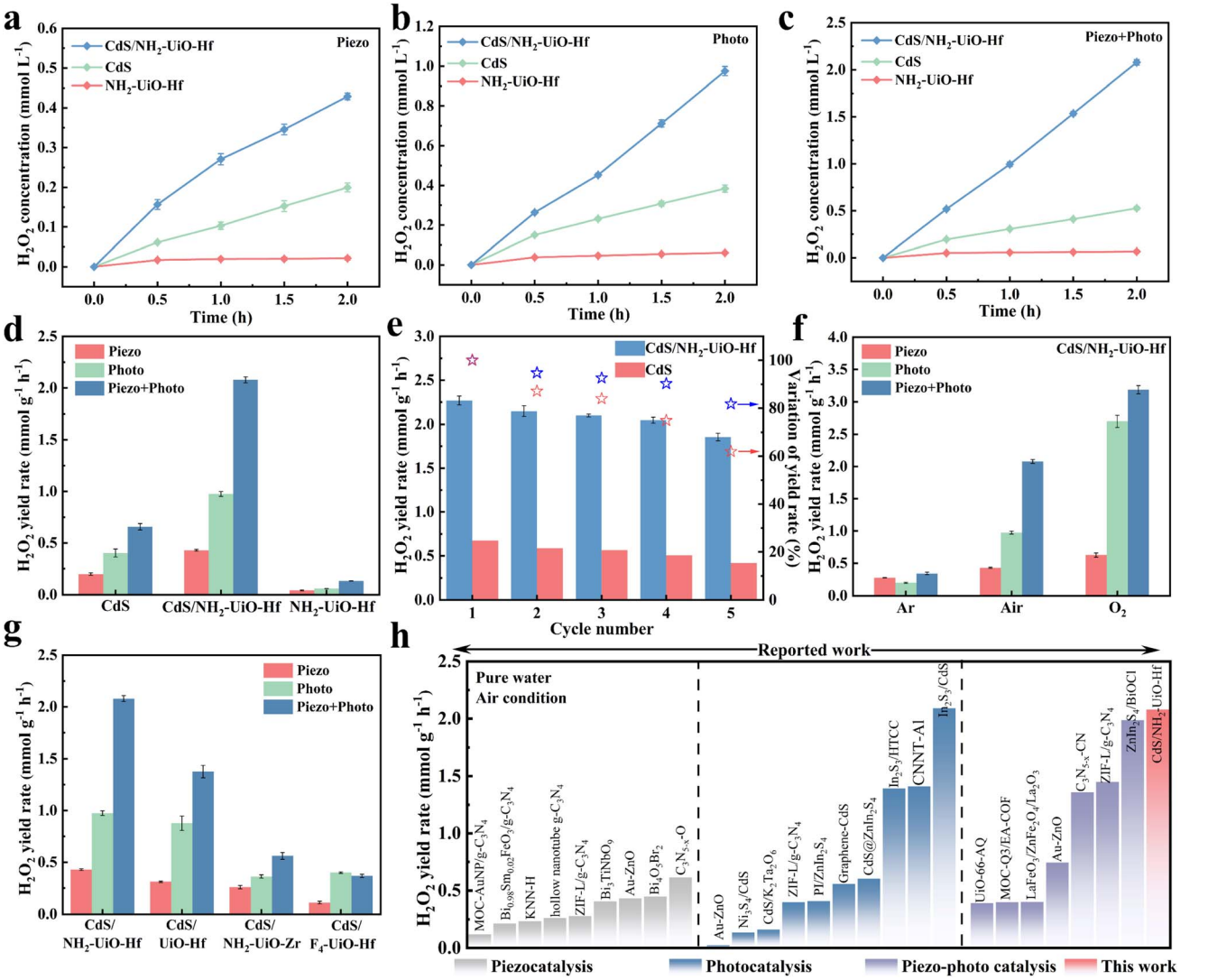

Fig. 3 Time-dependent H_2O_2 production for NH_2-UiO-Hf, CdS and CdS/NH_2-UiO-Hf under (a) ultrasonic vibration, (b) light radiation, and (c) simultaneous ultrasonic vibration and light radiation. (d) H_2O_2 yield rates of NH_2-UiO-Hf, CdS and CdS/NH_2-UiO-Hf. (e) Stability tests of CdS and CdS/NH_2-UiO-Hf. (f) H_2O_2 yield rates of CdS/NH_2-UiO-Hf under Ar, air and O_2 conditions. (g) H_2O_2 yield rates of heterostructures consisting of CdS and four model piezoelectric UiO-66-based MOFs. (h) Comparison of the H_2O_2 yield rates of CdS/NH_2-UiO-Hf with the reported catalysts.

were much higher than that of pristine CdS and NH_2-UiO-Hf under all three excitation conditions (*i.e.*, piezo, photo, and piezo-photo). And their yield rates under piezo-photocatalytic conditions are significantly enhanced compared to that under either piezocatalytic or photocatalytic conditions. Furthermore, the performance of mechanically mixed samples is far inferior to that of the heterostructure (Fig. S15), which indicates that the construction of heterojunctions is favorable for the enhanced catalytic activity. It is worth noting that the optimum H_2O_2 yield rate of CdS/NH_2-UiO-Hf under simultaneous ultrasonic vibration and light radiation reached up to 2079.1 μmol g^{-1} h^{-1}, which is 4.8 and 2.1 times higher than that under only ultrasonic vibration and light radiation, respectively. This suggests that the coupling of piezocatalytic and photocatalytic pathways significantly promotes H_2O_2 formation for CdS/NH_2-UiO-Hf. To reveal the stability of catalysts during the piezo-photocatalytic process, pristine CdS and CdS/NH_2-UiO-Hf heterostructure were tested under the same conditions (Fig. 3e). CdS/NH_2-UiO-Hf maintained more than 80% of the original yield rate after five cycle tests, while the rate of CdS dropped to 60%, manifesting that the heterostructure can effectively slow down the corrosion with improved stability. Thereafter, XRD and SEM analyses were carried out for CdS/NH_2-UiO-Hf after the stability test (Fig. S16) without noticeable changes compared to the as-prepared sample.

The H_2O_2 yield rates of CdS/NH_2-UiO-Hf under Ar, air and O_2 conditions were compared. As shown in Fig. 3f, the H_2O_2 production in an Ar-purged system was dramatically suppressed, while the H_2O_2 yield rate in an O_2-saturated system was increased compared to that under air conditions, which validates that the H_2O_2 yield predominantly originates from the ORR pathway. Subsequently, heterostructures consisting of CdS and various piezoelectric UiO-66-based MOFs were synthesised using the same methodology and tested for H_2O_2 production. The corresponding XRD patterns of these heterostructures are shown in Fig. S17. They showed pronounced variations in piezo-, photo- and piezo-photocatalytic H_2O_2 yield rates following the trend CdS/NH_2-UiO-Hf > CdS/UiO-Hf > CdS/NH_2-UiO-Zr > CdS/F_4-UiO-Hf (Fig. 1g and S18). This could result from the difference in light absorption, piezoelectricity, photogenerated carrier behaviors and SSA of the MOFs, which in turn affect the overall piezo-photocatalytic H_2O_2 production of the heterostructures. Collectively, the CdS/NH_2-UiO-Hf piezo-photocatalyst in water without scavengers and oxygen bubbling shows a performance advantage, compared to the state-of-the-art catalysts, as shown in Fig. 3h.[8,18–22,41–56]

2.4. Investigation of charge carrier behaviors

The charge separation and transfer behaviors of the catalysts were evaluated by transient photocurrent–time curves (TPC), electrochemical impedance spectroscopy (EIS) and steady-state photoluminescence (PL) spectroscopy. The TPC are shown in Fig. 4a, where the CdS/NH_2-UiO-Hf heterostructure demonstrated the highest currents under all piezo-, photo- and piezo-photocatalytic conditions. This implies efficient separation and transfer of carriers due to the formed heterojunction. In addition, it can be found that the currents of all catalysts under piezo-photocatalytic conditions are larger than those under either photocatalytic or piezocatalytic conditions, suggesting an increased quantity of electron–hole pairs upon coupling of the piezocatalytic and photocatalytic effects. Similarly, arc radii of the heterostructure in EIS are all much smaller than those of bare NH_2-UiO-Hf and CdS, indicative of its lowest charge transfer resistance (Fig. 4b). With respect to each sample, the arc radius under piezo-photocatalytic conditions is smaller than that under either piezocatalytic or photocatalytic conditions, revealing that the coupling effect of piezoelectricity and photocatalysis facilitates charge transfer. Furthermore, steady-state PL spectroscopy was conducted to unravel the radiative recombination dynamics of photogenerated carriers (Fig. 4c). The weaker PL intensity of CdS/NH_2-UiO-Hf than that of bare CdS implies a decreased radiative recombination of charges.

The optical properties and energy band structures of the catalysts were examined using UV-vis DRS, XPS and ultraviolet photoelectron spectroscopy (UPS) analysis. As shown in Fig. 4d, the catalysts have absorption edges in the range of 450–600 nm, presenting visible light absorption. In particular, the optical absorption edge of CdS/NH_2-UiO-Hf showed a redshift to 580 nm compared with that of bare CdS and NH_2-UiO-Hf. Meanwhile, the bandgaps of CdS and NH_2-UiO-Hf were determined to be 2.38 and 2.66 eV through the Tauc plots (inset of Fig. 4d). As shown in Fig. S19a and b, the secondary electron cut-off edges (E_C) of NH_2-UiO-Hf and CdS are 19.31 eV and 17.52 eV, respectively. Hence, according to the equation work function (WF) = 21.22 eV − E_C, their WFs are calculated to be 1.91 eV and 3.70 eV. Valence band (VB) XPS spectra further show that the VB to Fermi level (E_F) distances are 2.64 and 1.28 eV for NH_2-UiO-Hf and CdS, respectively (Fig. S19c and d). Using the equation $E_g = E_{VB} - E_{CB}$, VB and conduction band (CB) positions of NH_2-UiO-Hf are determined as 0.11 V and −2.55 V, respectively, and 0.54 V and −1.80 V for CdS.[57,58] The energy band structures of CdS and NH_2-UiO-Hf are illustrated in Fig. 4e. A schematic illustration of the charge transfer process of the CdS/NH_2-UiO-Hf heterojunction during piezo-photocatalysis is shown in Fig. 4f. Upon contact between CdS and NH_2-UiO-Hf, Fermi-level alignment leads to band bending and formation of a built-in electric field (IEF) at the heterojunction. Under illumination, the IEF drives the efficient separation of photogenerated electrons and holes, leading to the electrons migrating from CdS to NH_2-UiO-Hf to form a Z-scheme pathway for charge transfer. Under ultrasonic vibration, the piezoelectric polarization-intensified IEF further bends the energy bands, promoting carrier separation and transfer with suppressed recombination.[59–61]

2.5. The mechanism of piezo-photocatalysis

The piezoelectric properties of CdS, NH_2-UiO-Hf and CdS/NH_2-UiO-Hf coated on a Pt substrate were investigated using PFM. As shown in Fig. 5a, all samples displayed characteristic 180° phase reversal and amplitude–voltage hysteresis loops under applied DC bias for piezoelectric materials, which are quite different from the signals of the non-piezoelectric Pt substrate (Fig. S20).[62] The

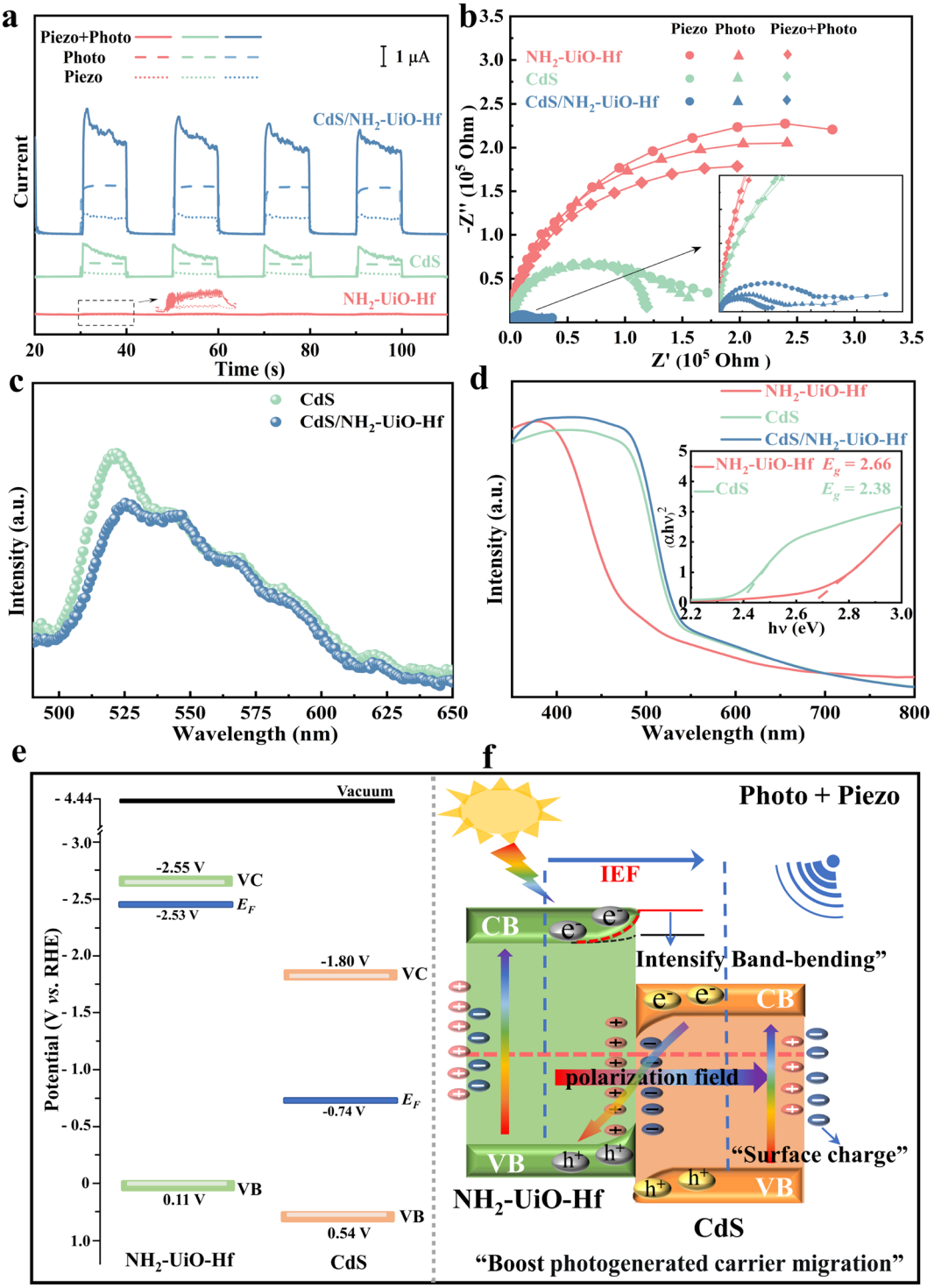

Fig. 4 (a) Transient photocurrent responses under piezo-, photo- and piezo-photocatalytic conditions. (b) EIS Nyquist plots, (c) steady-state PL spectra, (d) UV-vis DRS of the catalysts (inset: the corresponding Tauc plots). (e) Energy band structure of NH_2-UiO-Hf and CdS. (f) Schematic illustration of the charge transfer process of the CdS/NH_2-UiO-Hf heterojunction during piezo-photocatalysis.

d_{33} values were determined to be 78.31, 93.54, and 141.31 pm V^{-1} for NH_2-UiO-Hf, CdS and CdS/NH_2-UiO-Hf, respectively. The piezoelectricity of CdS/NH_2-UiO-Hf was considerably enhanced compared to that of bare CdS and NH_2-UiO-Hf, which could be ascribed to the increased structural asymmetry upon heterostructure assembly.[63] The corresponding PFM topography height, amplitude and phase images of CdS/NH_2-UiO-Hf are shown in Fig. 5b, c and S21. Additionally, the piezoelectric properties of NH_2-UiO-Hf, CdS and CdS/NH_2-UiO-Hf were further evaluated by fabricating piezoelectric nanogenerators (PENGs) (Fig. 5d). The open-circuit voltages (V_{oc}) generated by NH_2-UiO-Hf, CdS and CdS/NH_2-UiO-Hf under stimulation by an external force were 1.9

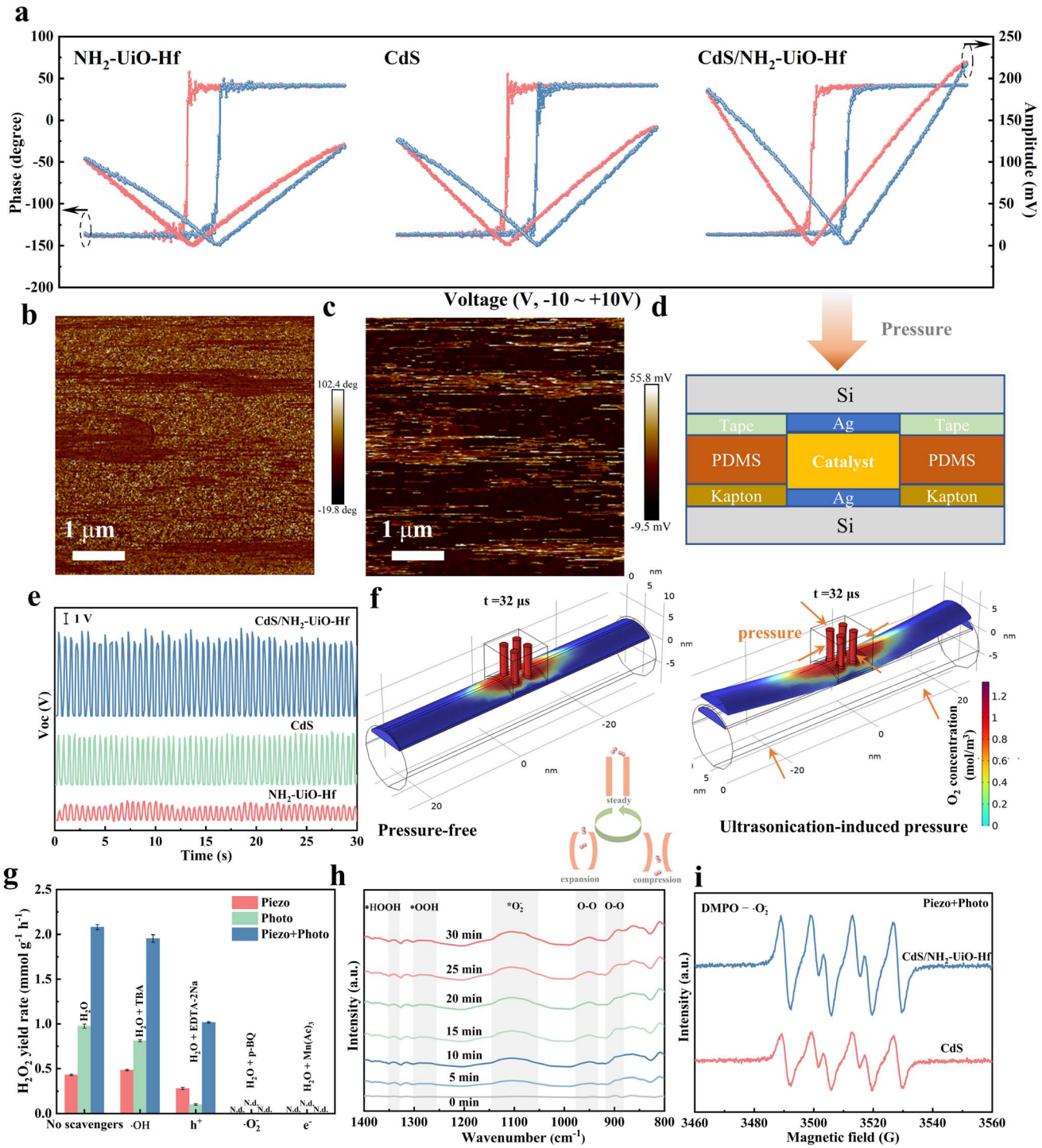

Fig. 5 (a) Piezoresponse amplitude–voltage and phase–voltage curves of NH_2-UiO-Hf, CdS and CdS/NH_2-UiO-Hf. PFM images of the (b) phase and (c) amplitude of CdS/NH_2-UiO-Hf. (d) Schematic diagram of the piezoelectric nanogenerator. (e) Open circuit voltages of the piezoelectric nanogenerator using NH_2-UiO-Hf, CdS and CdS/NH_2-UiO-Hf catalysts. (f) Finite element simulation results of O_2 transport in the hetero-structure under ultrasonication-induced cyclic deformation. (g) Piezo-photocatalytic H_2O_2 yield rates of CdS/NH_2-UiO-Hf during the trapping experiment of the active species. (h) *In situ* FTIR spectra of CdS/NH_2-UiO-Hf in deionized water under illumination. (i) EPR spectra of DMPO-$^{\bullet}O_2^-$ generated over CdS and CdS/NH_2-UiO-Hf during piezo-photocatalysis.

V, 5.2 V and 8.6 V, respectively (Fig. 5e), indicative of their good piezoelectric properties.

To unravel the mechano-fluidic regulation mechanism of a piezoelectric porous MOF under ultrasonic stimulation, a cubic model with dimensions of 8 × 8 × 8 nm^3 was used to represent the piezoelectric NH_2-UiO-Hf nanoparticle, while cylinders with a radius of 6 nm and a length of 58 nm were employed to simulate the CdS nanorod (Fig. S22). Coupled finite

element simulations (FESs) incorporating deformation, piezoelectricity, and mass transfer were performed on this heterostructure. The FES framework included dual boundary configurations: gas-phase simulations with top-inflow/open-flank boundaries and liquid-phase simulations with designated inlet/outlet pairs, enabling systematic comparison of O_2 transport in static *versus* dynamically deformed channels. By imposing ultrasonic-mimetic periodic deformation (static → tensile → compressive cycling), an enhancement in O_2 diffusion distance within the deformed channel was observed compared to the static control (Fig. 5f and S23), with accelerated concentration front propagation evidenced by gradient analysis. This enhancement stems from phase-synchronized pore volume modulation: tensile expansion generates negative pressure driving rapid external O_2 influx, while subsequent compression converts elastic energy into kinetic momentum for directional gas ejection. The corresponding surface stress distributions and piezo-potential distributions upon ultrasonic-induced deformation are shown in Fig. S24b, d and S25. The simulations also reveal that light irradiation influences the O_2 transfer process *via* the photothermal effect (Fig. S26). The light-induced heating drives non-isothermal diffusion, resulting in a noticeably higher O_2 concentration at the front end of the orifice by $t = 10$ s under illumination, in direct contrast to the low concentration observed without light (Fig. S27). Cumulative cycling effects facilitate mass transfer for the O_2 reduction reaction through stress-guided transport pathways, demonstrating that piezoelectric pore deformation triggers programmable microfluidic pumping for microenvironment engineering.

To investigate the piezo-photocatalytic reaction pathway towards H_2O_2 formation on CdS/NH_2-UiO-Hf, *tert*-butanol (TBA), EDTA-2Na, *p*-benzoquinone (*p*-BQ), and $Mn(Ac)_3$ were used as hydroxyl radical ($^{\bullet}OH$), hole (h^+), superoxide radical ($^{\bullet}O_2^-$) and electron (e^-) scavengers for the trapping experiment of active species. As shown in Fig. 5g, EDTA-2Na, $Mn(Ac)_3$ and *p*-BQ significantly suppressed the H_2O_2 yield, proving that h^+, e^- and $^{\bullet}O_2^-$ play a crucial role during the H_2O_2 formation process. The minor effect of TBA on H_2O_2 yield conclusively eliminates $^{\bullet}OH$ as a primary reaction intermediate. To further identify the key intermediates over CdS/NH_2-UiO-Hf during the formation of H_2O_2 under light illumination, the *in situ* FTIR spectrum was employed (Fig. 5h). The grey region exhibits progressively intensified peak signals with increasing reaction time. The O–O bond vibrational modes were observed at two distinct wavenumbers of 890 cm^{-1} and 948 cm^{-1}.[14,64] The peaks at 1106 cm^{-1}, 1290 cm^{-1} and 1342 cm^{-1} are attributed to $*O_2^-$, *OOH and $*H_2O_2$ intermediates, respectively.[22,65,66] In addition, prominent vibrational signatures of free H_2O_2 molecules were detected in the 2840–3062 cm^{-1} wavenumber range, providing direct evidence for successful H_2O_2 generation (Fig. S28).[64,66] To gain further insight into the key intermediate $^{\bullet}O_2^-$, electron paramagnetic resonance (EPR) was employed using 5,5-dimethyl-1-pyrroline *N*-oxide (DMPO) as the radical trapping agent. Fig. 5i illustrates that both CdS and CdS/NH_2-UiO-Hf exhibit the typical six-line characteristic peaks of DMPO-$^{\bullet}O_2^-$ under piezo-photocatalytic conditions, while the signal intensity of CdS/NH_2-UiO-Hf is much higher than that of bare CdS, suggesting the enhanced $^{\bullet}O_2^-$ generation through the incorporation of MOFs. Therefore, it can be concluded that the piezo-photocatalysis follows a two-step one-electron ORR pathway $O_2 \rightarrow *O_2^- \rightarrow *OOH \rightarrow *HOOH \rightarrow H_2O_2$.

3. Conclusions

In summary, based on the comprehensive investigation on a series of piezoelectric semiconducting MOFs with distinct metal nodes and substituents of the linker, we establish systematic design principles for engineering MOF-based piezo-photocatalysts with high activity. Further construction of heterojunctions consisting of the optimum MOF and another piezoelectric semiconductor results in a remarkably improved piezo-photocatalytic H_2O_2 yield rate of 2079.1 μmol g^{-1} h^{-1} in the absence of a sacrificial agent and O_2 bubbling. This performance enhancement originates from increased structural asymmetry with a stronger piezoelectric-induced built-in electric field, which drives the separation and migration of photogenerated electron–hole pairs participating in the subsequent redox reactions. Meanwhile, the piezoelectric effect-induced periodic deformation modulates the local microenvironment by improving gas capacities, diffusion kinetics, and O_2 activation within the micropores of MOFs. This work provides rational guidelines from initial MOF design to heterostructure post-assembly for developing highly active MOF-based piezo-photocatalysts.

Author contributions

G. L. and Y. L. conceived the idea. Y. L., L. G., J. Q. and J. L. conducted the experiments and analyzed the synthesis, performance and characterization data. M. Y., J. Z. and G. L. guided and supervised the conduct of this research and provided financial support. Y. L. and G. L. wrote the manuscript and B. S., M. Y., W. T., J. Z., and G. L. edited the manuscript. All authors discussed the results and commented on the manuscript.

Conflicts of interest

The authors declare no conflict of interest.

Data availability

The data supporting the findings of this work are available within the article and its supplementary information (SI). Raw data supporting the findings of this work are available from the corresponding author upon reasonable request. Supplementary information: materials, synthesis procedures, characterization, DFT calculations, supplementary performance testing, and finite element simulation results. See DOI: **https://doi.org/10.1039/d5sc07619f**.

Acknowledgements

This work was supported by the Fundamental Research Funds for the Central Universities in China. This work was also financially supported by the National Natural Science Foundation of China (No. 52172123). M. Y. acknowledges the support from the National Natural Science Foundation of China (Grant No. 52302302).

References

1 H. L. Hou, X. K. Zeng and X. W. Zhang, Production of Hydrogen Peroxide by Photocatalytic Processes, *Angew. Chem., Int. Ed.*, 2020, **59**, 17356–17376.

2 C. Yang, S. Wan, B. Zhu, J. Yu and S. Cao, Calcination–regulated Microstructures of Donor–Acceptor Polymers towards Enhanced and Stable Photocatalytic H_2O_2 Production in Pure Water, *Angew. Chem., Int. Ed.*, 2022, **61**, e202208438.

3 P. K. Cao, X. Quan, X. W. Nie, K. Zhao, Y. M. Liu, S. Chen, H. T. Yu and J. G. Chen, Metal single–site catalyst design for electrocatalytic production of hydrogen peroxide at industrial–relevant currents, *Nat. Commun.*, 2023, **14**, 172.

4 X. Zhang, D. Gao, B. Zhu, B. Cheng, J. Yu and H. Yu, Enhancing photocatalytic H_2O_2 production with Au co–catalysts through electronic structure modification, *Nat. Commun.*, 2024, **15**, 3212.

5 M. X. Zhang, H. C. Tao, C. Y. Zhai, J. L. Yang, Y. T. Zhou, D. H. Xia, G. Comodi and M. S. Zhu, Twin–brush ZnO mesocrystal for the piezo–activation of peroxymonosulfate to remove ibuprofen in water: Performance and mechanism, *Appl. Catal., B*, 2023, **326**, 122339.

6 C. X. Zhang, D. Lei, C. F. Xie, X. S. Hang, C. A. X. He and H. L. Jiang, Piezo–Photocatalysis over Metal–Organic Frameworks: Promoting Photocatalytic Activity by Piezoelectric Effect, *Adv. Mater.*, 2021, **33**, e2106308.

7 X. F. Zhou, B. Shen, J. W. Zhai and N. Hedin, Reactive Oxygenated Species Generated on Iodide–Doped $BiVO_4$/$BaTiO_3$ Heterostructures with Ag/Cu Nanoparticles by Coupled Piezophototronic Effect and Plasmonic Excitation, *Adv. Funct. Mater.*, 2021, **31**, 2009594.

8 Y. Y. Wen, H. A. Che, C. M. Tang, B. Liu and Y. H. Ao, A Schottky heterojunction with spatially separated active sites for piezo–photocatalytic dual–channel hydrogen peroxide generation, *Nano Energy*, 2024, **128**, 109837.

9 X. F. Zhou, F. Yan, B. Shen, J. W. Zhai and N. Hedin, Enhanced Sunlight–Driven Reactive Species Generation via Polarization Field in Nanopiezoelectric Heterostructures, *ACS Appl. Mater. Interfaces*, 2021, **13**, 29691–29707.

10 X. F. Zhou, F. Yan, A. Lyubartsev, B. Shen, J. W. Zhai, J. C. Conesa and N. Hedin, Efficient Production of Solar Hydrogen Peroxide Using Piezoelectric Polarization and Photoinduced Charge Transfer of Nanopiezoelectrics Sensitized by Carbon Quantum Dots, *Adv. Sci.*, 2022, **9**, e2105792.

11 Z. Li, Y. Y. Zhou, Y. T. Zhou, K. Wang, Y. Yun, S. Y. Chen, W. T. Jiao, L. Chen, B. Zou and M. S. Zhu, Dipole field in nitrogen–enriched carbon nitride with external forces to boost the artificial photosynthesis of hydrogen peroxide, *Nat. Commun.*, 2023, **14**, 5742.

12 W. Zhong, A. Y. Meng, Y. R. Su, H. G. Yu, P. G. Han and J. G. Yu, Achieving Free–Electron Transfer Reversal and dz^2–Orbital Occupancy Modulation on Core–shell NiS@Au Cocatalysts for Highly Selective H_2O_2 Photosynthesis, *Angew. Chem., Int. Ed.*, 2025, **64**, e202425038.

13 Z. Li, Z. Dong, Z. Zhang, B. Wei, C. Meng, W. Zhai, Y. Wang, X. Cao, B. Han and Y. Liu, Covalent Organic Frameworks for Boosting H_2O_2 Photosynthesis via the Synergy of Multiple Charge Transfer Channels and Polarized Field, *Angew. Chem., Int. Ed.*, 2024, **64**, e202420218.

14 D. Jiao, C. Ding, M. Xu, X. Ruan, S. K. Ravi and X. Cui, Modulating Yeager Adsorption Configuration of O_2 Through Cd Doping in $Zn_3In_2S_6$ for Photosynthesis of H_2O_2, *Adv. Funct. Mater.*, 2024, **35**, 2416753.

15 X. Zhang, H. Su, P. Cui, Y. Cao, Z. Teng, Q. Zhang, Y. Wang, Y. Feng, R. Feng, J. Hou, X. Zhou, P. Ma, H. Hu, K. Wang, C. Wang, L. Gan, Y. Zhao, Q. Liu, T. Zhang and K. Zheng, Developing Ni single–atom sites in carbon nitride for efficient photocatalytic H_2O_2 production, *Nat. Commun.*, 2023, **14**, 7115.

16 X. Ruan, S. Zhao, M. Xu, D. Jiao, J. Leng, G. Fang, D. Meng, Z. Jiang, S. Jin, X. Cui and S. K. Ravi, Iso–Elemental $ZnIn_2S_4$/$Zn_3In_2S_6$ Heterojunction with Low Contact Energy Barrier Boosts Artificial Photosynthesis of Hydrogen Peroxide, *Adv. Energy Mater.*, 2024, **14**, 2401744.

17 T. Liu, Z. Pan, J. J. M. Vequizo, K. Kato, B. Wu, A. Yamakata, K. Katayama, B. Chen, C. Chu and K. Domen, Overall photosynthesis of H_2O_2 by an inorganic semiconductor, *Nat. Commun.*, 2022, **13**, 1034.

18 E. H. Zhang, Q. H. Zhu, J. H. Huang, J. Liu, G. Q. Tan, C. J. Sun, T. Li, S. Liu, Y. M. Li, H. Z. Wang, X. D. Wan, Z. H. Wen, F. T. Fan, J. T. Zhang and K. Ariga, Visually resolving the direct Z–scheme heterojunction in CdS@$ZnIn_2S_4$ hollow cubes for photocatalytic evolution of H_2 and H_2O_2 from pure water, *Appl. Catal., B*, 2021, **293**, 120213.

19 Y. R. Wang, J. J. Zhao, W. Q. Hou and Y. M. Xu, Decoration of CdS nanowires with Ni_3S_4 nanoballs enhancing H_2 and H_2O_2 production under visible light, *Appl. Catal., B*, 2022, **310**, 121350.

20 B. S. Jiang, D. Y. Chen, N. J. Li, Q. F. Xu, H. Li and J. M. Lu, Graphene–Encapsulated CdS as a High–Performance Photocatalyst for H_2O_2 Production from Pure Water, *Ind. Eng. Chem. Res.*, 2023, **62**, 12974–12984.

21 C. Lai, M. Xu, F. Xu, B. Li, D. Ma, Y. Li, L. Li, M. Zhang, D. Huang, L. Tang, S. Liu, H. Yan, X. Zhou, Y. Fu and H. Yi, An S–scheme CdS/$K_2Ta_2O_6$ heterojunction photocatalyst for production of H_2O_2 from water and air, *Chem. Eng. J.*, 2023, **452**, 139070.

22 J. D. Hu, B. R. Li, X. Li, T. Y. Yang, X. G. Yang, J. F. Qu, Y. H. Cai, H. B. Yang and Z. Q. Lin, Lattice Match–Enabled Covalent Heterointerfaces with Built–in Electric Field for Efficient Hydrogen Peroxide Photosynthesis, *Adv. Mater.*, 2024, **36**, 2412070.

23 G. Y. Liu, W. S. Y. Wong, M. Kraft, J. W. Ager, D. Vollmer and R. Xu, Wetting–regulated gas–involving (photo) electrocatalysis: biomimetics in energy conversion, *Chem. Soc. Rev.*, 2021, **50**, 10674–10699.

24 B. Cao, Y. F. Liu, Y. Zhao, J. S. Qu, Q. Zhou, F. S. Xiao, C. Li, L. Wang and R. G. Li, Zeolite Encapsulation to Enhance Interfacial Gas Availability for Photocatalytic Hydrogen Peroxide Production, *Angew. Chem., Int. Ed.*, 2025, **64**, e202422495.

25 D. Moitra, A. Ganesan, F. Wang, L. Q. Qiu, K. Siniard, Z. Z. Yang, S. M. Mahurin, L. L. He, K. Li, H. J. Liu, D. E. Jiang, T. Wang and S. Dai, Permanent Nanobubbles in Water: Liquefied Hollow Carbon Spheres Break the Limiting Diffusion Current of Oxygen Reduction Reaction, *J. Am. Chem. Soc.*, 2025, **147**, 3421–3427.

26 D. P. Erdosy, M. B. Wenny, J. Cho, C. DelRe, M. V. Walter, F. Jiménez-Angeles, B. F. Qiao, R. Sanchez, Y. F. Peng, B. D. Polizzotti, M. O. De la Cruz and J. A. Mason, Microporous water with high gas solubilities, *Nature*, 2022, **608**, 712.

27 W. Zhang, M. Y. Dai, Z. L. Z. Zeng, Y. H. Wang, Y. Zhang, W. P. Ni, S. Y. Wang and S. G. Zhang, Electrolyte Design Using "Porous Water" for High–purity Carbon Monoxide Electrosynthesis from Dilute Carbon Dioxide, *Angew. Chem., Int. Ed.*, 2025, **64**, e202424104.

28 Y. Cheng, Q. Li, M. I. B. Salaman, C. Wei, Q. Wang, X. Ma, B. Liu and A. B. Wong, Microenvironment Tailoring for Electrocatalytic CO_2 Reduction: Effects of Interfacial Structure on Controlling Activity and Selectivity, *J. Am. Chem. Soc.*, 2025, **147**, 12438–12448.

29 L. H. Cai, J. J. Du, F. P. Han, T. C. Shi, H. Zhang, Y. Lu, S. R. Long, W. Sun, J. L. Fan and X. J. Peng, Piezoelectric Metal–Organic Frameworks Based Sonosensitizer for Enhanced Nanozyme Catalytic and Sonodynamic Therapies, *ACS Nano*, 2023, **17**, 7901–7910.

30 H. Hu, X. Li, K. Zhang, G. Yan, W. Kong, A. Qin, Y. Ma, A. Li, K. Wang, H. Huang, X. Sun and T. Ma, Dual Modification of Metal–Organic Frameworks for Exceptional High Piezo–Photocatalytic Hydrogen Production, *Adv. Mater.*, 2025, **37**, 2419023.

31 S. Y. Zhao, M. S. Liu, Y. Q. Zhang, Z. C. Zhao, Q. Z. Zhang, Z. L. Mu, Y. K. Long, Y. H. Jiang, Y. Liu, J. M. Zhang, S. Li, X. J. Zhang and Z. T. Zhang, Harvesting mechanical energy for hydrogen generation by piezoelectric metal–organic frameworks, *Mater. Horiz.*, 2022, **9**, 1978–1983.

32 Y. Wang, W. Lin, S. Yu, X. Huang, X. Lang, Q. He, L. Gao, H. Zhu and J. Chen, A biocompatible Zr–based metal–organic framework UiO–66–PDC as an oral drug carrier for pH–response release, *J. Solid State Chem.*, 2021, **293**, 121805.

33 H. Liu, M. Cheng, Y. Liu, G. Zhang, L. Li, L. Du, B. Li, S. Xiao, G. Wang and X. Yang, Modified UiO–66 as photocatalysts for boosting the carbon–neutral energy cycle and solving environmental remediation issues, *Coord. Chem. Rev.*, 2022, **458**, 214428.

34 M. Wu, Q. Zhang, Q. Zhang, H. Wang, F. Wang, J. Liu, L. Guo and K. Song, Research Progress of UiO–66–Based Electrochemical Biosensors, *Front. Chem.*, 2022, **10**, 842894.

35 Y. Sun, J. Gao, Y. Cheng, Y.-W. Zhang and K. Zeng, Design of the Hybrid Metal–Organic Frameworks as Potential Supramolecular Piezo–/Ferroelectrics, *J. Phys. Chem. C.*, 2019, **123**, 3122–3129.

36 M. H. Beyzavi, R. C. Klet, S. Tussupbayev, J. Borycz, N. A. Vermeulen, C. J. Cramer, J. F. Stoddart, J. T. Hupp and O. K. Farha, A Hafnium–Based Metal–Organic Framework as an Efficient and Multifunctional Catalyst for Facile CO_2 Fixation and Regioselective and Enantioretentive Epoxide Activation, *J. Am. Chem. Soc.*, 2014, **136**, 15861–15864.

37 W. J. Zheng, K. H. Bowen, J. Li, I. Dabkowska and M. Gutowski, Electronic Structure Differences in ZrO_2 vs HfO_2, *J. Phys. Chem. A*, 2005, **109**, 11521–11525.

38 Y. Sun, Z. G. Hu, D. Zhao and K. Y. Zeng, Probing nanoscale functionalities of metal–organic framework nanocrystals, *Nanoscale*, 2017, **9**, 12163–12169.

39 X. Ruan, M. Xu, C. Ding, J. Leng, G. Fang, D. Meng, W. Zhang, Z. Jiang, S. K. Ravi, X. Cui and J. Yu, Cd Single Atom as an Electron Mediator in an S–Scheme Heterojunction for Artificial Photosynthesis of H_2O_2, *Adv. Energy Mater.*, 2025, 2405478.

40 S. Lin, S. Sun, X. Zhang, H. Tang, J. Liu and X. Li, Piezo–Photocatalytically Induced Dual–Channel Pathway of $Cd_xZn_{1-x}S$ Solid–Solution Nanorods for Hydrogen Peroxide Evolution, *Adv. Mater. Technol.*, 2024, **10**, 2401133.

41 L. X. Zhang, K. Wang, Y. Q. Jia, L. P. Fang, C. Han, J. Q. Li, Z. P. Shao, X. Y. Li, J. S. Qiu and S. M. Liu, Self–Assembled $LaFeO_3/ZnFe_2O_4/La_2O_3$ Ultracompact Hybrids with Enhanced Piezo–Phototronic Effect for Oxygen Activation in Ambient Conditions, *Adv. Funct. Mater.*, 2022, **32**, 2205121.

42 C. Fu, T. Wu, G. Sun, G. Yin, C. Wang, G. Ran and Q. Song, Dual–defect enhanced piezocatalytic performance of C_3N_5 for multifunctional applications, *Appl. Catal., B*, 2023, **323**, 122196.

43 C. Fu, M. Y. Zhao, X. Chen, G. W. Sun, C. Wang and Q. J. Song, Unraveling the dual defect effects in C_3N_5 for piezo–photocatalytic degradation and H_2O_2 generation, *Appl. Catal., B*, 2023, **332**, 122752.

44 M. Fu, J. H. Luo, B. Shi, S. C. Tu, Z. H. Wang, C. L. Yu, Z. Q. Ma, X. Y. Chen and X. M. Li, Promoting Piezocatalytic H_2O_2 Production in Pure Water by Loading Metal–Organic Cage–Modified Gold Nanoparticles on Graphitic Carbon Nitride, *Angew. Chem., Int. Ed.*, 2024, **63**, e202316346.

45 C. Y. Wang, C. Hu, F. Chen, H. T. Li, Y. H. Zhang, T. Y. Ma and H. W. Huang, Polar Layered Bismuth–Rich Oxyhalide Piezoelectrics $Bi_4O_5X_2$ (X=Br, I): Efficient Piezocatalytic Pure Water Splitting and Interlayer Anion–Dependent Activity, *Adv. Funct. Mater.*, 2023, **33**, 2301144.

46 K. Wang, Z. Shu, J. Zhou, Z. L. Zhao, Y. C. Wen and S. X. Sun, Enhancing piezocatalytic H_2O_2 production through morphology control of graphitic carbon nitride, *J. Colloid Interface Sci.*, 2023, **648**, 242–250.

47 Y. F. Cui, F. H. Wang, P. P. Yuan, W. Liu, B. Y. Fang, Z. Wang and Y. P. Pu, Harvesting Vibration Energy to Produce

Hydrogen Peroxide with Bi_3TiNbO_9 Nanosheets through a Water Oxidation Dominated Dual–Channel Pathway, *ACS Sustainable Chem. Eng.*, 2024, **12**, 3595–3607.

48 Z. Z. Liang, X. A. Li, Q. Z. Chen, X. L. Wang, P. Y. Su, J. F. Huang, Y. C. Zhou, L. M. Xiao and J. M. Liu, A Direct Z–Scheme Single–Atom MOC/COF Piezo–Photocatalytic System for Overall Water Splitting, *ACS Catal.*, 2024, **14**, 10447–10461.

49 X. Liu, X. Dong, Y. Wang, J. Gao, N. Zheng and X. Zhang, Polyimide/$ZnIn_2S_4$ heterostructures toward outstanding photocatalytic H_2O_2 production from pure water and air, *Appl. Surf. Sci.*, 2024, **643**, 158637.

50 L. Meng, C. Zhao, X. Zhang, R. Guo, Y. Zheng, H. Chu, H. Fu, P. Wang and C. –C. Wang, Piezo–photocatalytic synergetic for H_2O_2 generation via dual–pathway over Z–scheme ZIF–L/g–C_3N_4 heterojunction, *Nano Energy*, 2024, **128**, 109795.

51 X. M. Sun, K. L. Lv, F. Liu, P. Wang, K. J. Zhang, J. W. Zhang and P. Chen, Insight into interfacial engineering for enhancing the synergistic effect of piezo–photocatalytic hydrogen peroxide production, *Chem. Eng. J.*, 2024, **497**, 154504.

52 H. Tan, P. Zhou, M. Liu, Y. Gu, W. Chen, H. Guo, J. Zhang, K. Yin, Y. Zhou, C. Shang, Q. Zhang, L. Gu, N. Zhang, J. Ma, Z. Zheng, M. Luo and S. Guo, Al–N_3 Bridge Site Enabling Interlayer Charge Transfer Boosts the Direct Photosynthesis of Hydrogen Peroxide from Water and Air, *J. Am. Chem. Soc.*, 2024, **146**, 31950–31960.

53 X. L. Tang, C. L. Yu, J. M. Zhang, K. W. Liu, D. B. Zeng, F. Li, F. Li, G. J. Ma, Y. B. Jiang and Y. F. Zhu, Furan–Based HTCC/In_2S_3 Heterojunction Achieves Fast Charge Separation To Boost the Photocatalytic Generation of H_2O_2 in Pure Water, *ACS Catal.*, 2024, **14**, 16245.

54 H. Zeng, C. B. Liu, B. X. Lan, M. X. Tan, C. Y. Yu, Y. J. Su, L. J. Qiao and Y. Bai, Bifunctional $Bi_{0.98}Sm_{0.02}FeO_3$/g–C_3N_4 Piezocatalyst for Simultaneous H_2 and H_2O_2 Production, *ACS Appl. Mater. Interfaces*, 2024, **16**, 70566.

55 C. Chen, K. Y. Gu, P. F. Wang, Z. Q. Liu and Y. H. Ao, Spatially Separated Redox Centers in Anthraquinone–grafted Metal–Organic Frameworks for Efficient Piezo–photocatalytic H_2O_2 Production, *Angew. Chem., Int. Ed.*, 2025, **64**, e202425656.

56 X. Wang, X. Wei, Q. Su, D. Wang, X. Wang, Q. Chen, X. Lv and J. Wu, Terraced (K, Na)NbO_3 piezocatalysts with superior H_2O_2 production, *Nano Energy*, 2025, **133**, 110459.

57 G. Wu, W. Zhang, Z. Mo, X. Zhao, P. Sun, Q. Wang, P. Yan, X. She and H. Xu, S–Scheme Homojunction Carbon Nitride for Photocatalytic Overall Water Splitting, *ACS Catal.*, 2025, **15**, 8822–8832.

58 X. Zhai, Z. Wei, Z. Lu, X. Zhang, X. Chen, Y. Liu, J. Deng, Y. Zhu, H. Dai and L. Jing, Cobalt Single Atom–Enhanced Photocatalysis: Hetero–Phase Elemental Phosphorus for Visible Light Hydrogen Production from Pure Water Splitting, *Adv. Funct. Mater.*, 2025, **38**, e202503667.

59 S. Tu, Y. Guo, Y. Zhang, C. Hu, T. Zhang, T. Ma and H. Huang, Piezocatalysis and Piezo–Photocatalysis: Catalysts Classification and Modification Strategy, Reaction Mechanism, and Practical Application, *Adv. Funct. Mater.*, 2020, **30**, 2005158.

60 X. F. Zhou, B. Shen, A. Lyubartsev, J. W. Zhai and N. Hedin, Semiconducting piezoelectric heterostructures for piezo– and piezophotocatalysis, *Nano Energy*, 2022, **96**, 107141.

61 Y. Zhao, T. Huang, X. Zhang, Y. Cui, L. Zhang, L. Li and Z. L. Wang, Piezotronic and piezo–phototronic effects on sonodynamic disease therapy, *BMEMat*, 2023, **1**, e12006.

62 Q. Q. Yang, J. C. Hu, Y. W. Fang, Y. Y. Jia, R. Yang, S. Q. Deng, Y. Lu, O. Dieguez, L. L. Fan, D. X. Zheng, X. X. Zhang, Y. Q. Dong, Z. L. Luo, Z. Wang, H. H. Wang, M. L. Sui, X. R. Xing, J. Chen, J. J. Tian and L. X. Zhang, Ferroelectricity in layered bismuth oxide down to 1 nanometer, *Science*, 2023, **379**, 1218–1224.

63 J. Z. Liu, X. F. Zhou, J. Qian, S. M. Wang, S. Y. Ma, B. Shen, W. G. Tu, R. Xu, G. Y. Liu and J. W. Zhai, Polarization Boosted Solar H_2O_2 Production over Quantum Dot–Decorated Nanosheets with Rich Oxygen Vacancies, *ACS Sustainable Chem. Eng.*, 2023, **11**, 18089–18101.

64 Y. H. Liu, X. X. Deng, Y. Wang, Q. Luo, Y. X. Liu, S. F. Yin and P. Chen, Unveiling Intrinsic Charge Transfer Dynamics in Bone–Joint S–Scheme Heterostructures To Promote Photocatalytic Hydrogen Peroxide Generation, *ACS Catal.*, 2024, **14**, 16287–16296.

65 W. Wang, Z. Chen, C. Li, B. Cheng, K. Yang, S. Zhang, G. Luo, J. Yu and S. Cao, Graphene Quantum Dot–Modified $Mn_{0.2}Cd_{0.8}S$ for Efficient Overall Photosynthesis of H_2O_2, *Adv. Funct. Mater.*, 2025, 2422307.

66 Z. P. Xie, X. Chen, W. B. Wang, X. T. Ke, X. R. Zhang, S. B. Wang, X. F. Wu, J. C. Yu and X. C. Wang, Variation of Chemical Microenvironment of Pores in Hydrazone–Linked Covalent Organic Frameworks for Photosynthesis of H_2O_2, *Angew. Chem., Int. Ed.*, 2024, **63**, e202410179.

